

Passage times and friction due to flow of confined cancer cells, drops, and deformable particles in a microfluidic channel

This content has been downloaded from IOPscience. Please scroll down to see the full text.

2017 Converg. Sci. Phys. Oncol. 3 024001

(<http://iopscience.iop.org/2057-1739/3/2/024001>)

View [the table of contents for this issue](#), or go to the [journal homepage](#) for more

Download details:

IP Address: 106.51.223.184

This content was downloaded on 01/04/2017 at 14:58

Please note that [terms and conditions apply](#).

You may also be interested in:

[Single cell metastatic phenotyping using pulsed nanomechanical indentations](#)

Hesam Babahosseini, Jeannine S Strobl and Masoud Agah

[Real-time control of a microfluidic channel for size-independent deformability cytometry](#)

Guofeng Guan, Peter C Y Chen, Weng Kung Peng et al.

[Microfluidic channel for characterizing normal and breast cancer cells](#)

T N TruongVo, R M Kennedy, H Chen et al.

[Cellular-scale hydrodynamics](#)

Manouk Abkarian, Magalie Faivre, Renita Horton et al.

[The fundamental role of mechanical properties in the progression of cancer disease and inflammation](#)

Claudia Tanja Mierke

[Droplet based microfluidics](#)

Ralf Seemann, Martin Brinkmann, Thomas Pfohl et al.

[Advances in the microrheology of complex fluids](#)

Thomas Andrew Waigh

[Active elastic thin shell theory for cellular deformations](#)

Hélène Berthoumieux, Jean-Léon Maître, Carl-Philipp Heisenberg et al.

[Cell mechanics: a dialogue](#)

Jiaxiang Tao, Yizeng Li, Dhruv K Vig et al.

Convergent Science Physical Oncology



PAPER

Passage times and friction due to flow of confined cancer cells, drops, and deformable particles in a microfluidic channel

RECEIVED
27 September 2016

REVISED
9 December 2016

ACCEPTED FOR PUBLICATION
9 February 2017

PUBLISHED
29 March 2017

Zeina S Khan^{1,2}, Nabiollah Kamyabi², Fazle Hussain¹ and Siva A Vanapalli²

¹ Mechanical Engineering, Texas Tech University, Lubbock, TX 79409, United States of America

² Chemical Engineering, Texas Tech University, Lubbock, TX 79409, United States of America

E-mail: siva.vanapalli@ttu.edu

Keywords: cancer, metastasis, microfluidics, friction, cell mechanics

Abstract

The confined flow of cancer cells, viscous droplets, and deformable, elastic particles in microchannels at millisecond deformation timescales show that the passage time and friction force depend on cell, droplet, and particle size and viscosity of the emulsion droplets, but not on the elastic modulus of particles, contrary to prior claims. Force balance reveals a viscosity-dependent lubrication film thickness larger than 100 nm in the majority of cases, indicating that hydrodynamic friction and not surface friction dominates cell and deformable particle transport. Our results suggest that—in the hydrodynamic friction regime—cancer cell transport through microchannels is similar to that of drops. Given that prior works report passage times and cell velocities that vary by five orders of magnitude, we emphasize the need to comprehensively understand the relationship between cell confinement, velocity, friction force, lubrication film thickness, and rheology to interpret tumor cell passage time data and connect it to cancer cell invasiveness.

Introduction

An important step in cancer metastasis is the transport of tumor cells by blood flow to distant organs [1, 2]. *In vivo* studies have shown that despite being larger than the capillary diameter, cells can squeeze through microcapillaries with velocities ranging from 1–100 $\mu\text{m s}^{-1}$ [3]. Identifying the cell mechanical properties and the hydrodynamic mechanisms controlling cancer cell transport through microcapillaries is important not only for basic understanding of metastasis but also for *ex vivo* microfluidic characterization of malignant cells and differentiating them from non-malignant cells [4–9].

There are several parameters that can influence the passage of cancer cells through capillaries. For a given pressure drop along a capillary, the transit velocity of the cell through the capillary is determined by its degree of confinement, rheology, or deformability, and the frictional interactions with the wall. Moreover, the transit velocity sets the cellular deformation timescale (or deformation rate), which could in turn impact its rheology since cells are viscoelastic bodies. Understanding the complex relationships among cellular confinement, rheology, friction, and deformation rate is crucial to develop the metrics to distinguish metastatic and non-metastatic cells and elucidate the role of cellular mechanical properties in tumor cell transport.

A simple method to study passage of tumor cells through capillaries is to use constricted microfluidic channels where the key observable is the transit velocity (V) or passage time (τ_p) [7, 9–15]. $\tau_p = L_{\text{CH}}/V$ is defined as the time needed to traverse the full length of the constricted channel (L_{CH}). Previous studies using the passage time as a metric for cancer cell invasive potential produced conflicting results. For example, Guan *et al* [12], have shown the malignant breast cancer cells (MCF-7) to have different passage times than the benign (MCF-10A) cells, while Hou *et al* [7] found no difference in the passage times of the two cell lines. This disagreement highlights the need to understand in detail how cell mechanical properties and friction influence the tumor cell passage time.

For a cell moving with a constant velocity, the balance between the pressure force that pushes the cell forward and the friction force that resists motion determines the passage time. Depending on the thickness of the lubricating film layer (δ) between the cell surface and channel wall, two distinct friction regimes are expected. For $\delta = \mathcal{O}(10)\text{ nm}$, friction with channel walls is expected to depend on intermolecular and surface interactions [16]. Alternatively, for $\delta \geq 100\text{ nm}$, the friction force depends on hydrodynamic shear stress in the lubricating film. The magnitude of the film thickness is set by both the cell velocity and its rheological properties.

The above general picture of friction regimes and how lubrication film thickness (δ) depends on velocity and mechanical properties has not been established for cells. Most experiments to date [7, 9–15, 17] have measured only the passage time or cell velocity, and friction force or δ measurements are very scarce. The only study that measured δ of a cell during passage through a microchannel is that of Preira *et al* [18]. Using reflectance interference contrast microscopy, they reported $\delta \approx 70$ nm for cell velocities of 100–1000 $\mu\text{m s}^{-1}$, suggesting that surface forces are important in setting the cell passage time. Given that prior work reported passage times ($\tau_p \approx 1$ ms–100 s) and cell velocities ($V \approx -100\,000$ $\mu\text{m s}^{-1}$) varying over five orders of magnitude (see the discussion section), more studies are clearly needed to measure friction forces and δ .

An important parameter that can influence passage time, friction, and δ is cell mechanical properties. It has been argued that the cell elastic modulus sets the passage time since stiffer objects push more strongly against channel walls, reducing their lubricating film thickness and velocity, and increasing their passage times [9, 11, 13, 17]. This picture has been tested with cells moving relatively slowly ($\tau_p \approx 1$ –100 s, $V \approx 23$ –2300 $\mu\text{m s}^{-1}$), and supporting evidence came from drug-induced stiffening of the actin cytoskeleton [11]. It is not known if the elastic modulus also sets the passage time when cells are moving at higher velocities. It is plausible that mechanical properties other than the elastic modulus affect the passage time at short timescales as the cell rheological response depends on both the deformation magnitude and the rate [19, 20].

Here, we investigate the passage time of cancer cells at short timescales ($\tau_p \approx 1$ –10 ms), by forcing them through constricted microchannels at velocities of 4–300 mm s^{-1} , that are at least an order of magnitude higher than previous studies. This velocity range is on the high side of cell speeds from *in vivo* microcapillary blood flow, which range from 0.001–10 mm s^{-1} [3, 21]. Unlike prior passage-time studies, we also test synthetic droplets and deformable particles with well-defined mechanical properties to interpret the cell data. Previously, cells were variously modeled by viscous drops, viscoelastic materials with constant cortical tension, and elastic particles [22]. Since interfacial tension and viscosity can both contribute to the deformation of a viscous drop in a flow [23], and the elastic modulus of a viscoelastic object can influence its passage time through a capillary [24], we tested emulsion droplets of varying viscosity and interfacial tension, as well as elastic particles with different elastic moduli. By integrating a microfluidic manometer downstream of the constricted microchannel [8, 25–27], we also measured the friction force acting on the cells and deformable particles to assess how friction forces and lubrication film thicknesses vary as functions of particle confinement, viscosity, interfacial tension, and elastic modulus.

Table 1. Constricted channel dimensions and samples used.

Constriction H \times W \times L	Samples
9 $\mu\text{m} \times 8 \mu\text{m} \times 190 \mu\text{m}$	CCRF-CEM, CCRF-CEM LatA, Jurkat, PDMS particles, hexadecane and silicone oil emulsions
12 $\mu\text{m} \times 12.4 \mu\text{m} \times 350 \mu\text{m}$	LNCAp, CL-1, CL-2
11 $\mu\text{m} \times 15 \mu\text{m} \times 286 \mu\text{m}$	A172
11 $\mu\text{m} \times 15 \mu\text{m} \times 238 \mu\text{m}$	1321N1, benign glial cells

The key findings of our work are: (i) droplet viscosity and not particle elastic modulus influences passage time, (ii) droplet viscosity and not particle elastic modulus affects the friction force and lubrication film thickness, (iii) at millisecond timescales and large deformation rates hydrodynamic friction regulates cancer cell transport and not surface friction, and (iv) the friction force and lubrication film thickness of different cancer cells lie closer to those of droplets suggesting that, under our operating conditions, cancer cell and viscous droplet flow through microchannels are similar. We conclude with a discussion on the implications of our findings for using passage time as a metric for cell deformability and cancer cell invasive potential.

Materials and methods

Cell culture and preparation

All cells were cultured in an incubator at 37 °C with a 5% CO₂ atmosphere. Non-adherent CCRF-CEM and Jurkat leukemia cells were cultured in RPMI-1640 medium. Medium supplements for CCRF-CEM cells were 10% fetal bovine serum (FBS) and 0.1% insulin-transferrin selenium. Supplements for Jurkat cells were 1% Penicillin-Streptomycin (Gibco 15140-148) and 10% FBS. Latrunculin A treated CCRF-CEM cells (CCRF-CEM LatA) were incubated with 200 nM Latrunculin A in RPMI-1640 medium for 2 h.

Prostate cancer cell lines of different metastatic potential were chosen. CL-1 and CL-2 are highly metastatic and LNCAp is lowly metastatic [29]. All three cell lines were cultured in RPMI-1640 medium. The supplements for LNCAp cells were 5% FBS, 2 mM L-Glutamine, non-essential amino acids, 1 mM Sodium Pyruvate, and 1% Penicillin/Streptomycin. The supplements for the CL-1 cell line were the same as for CL-2 and LNCAp except, in place of 5% FBS, 5% charcoal-treated FBS was used. A172 glioblastoma, 1321N1 astrocytoma, and benign human glial (L0329, L0367) cell lines were cultured as previously described [8]. All adherent cells were harvested for experiments using a Trypsin/EDTA solution (ScienCell 0103), centrifuged, and suspended in a 2:1 solution of Trypan Blue cell death marker and growth medium. Trypan Blue was used to exclude dead cells from analysis. Leukemia cells were used with a concentration of 6×10^5 cells mL^{-1} , prostate cancer cells

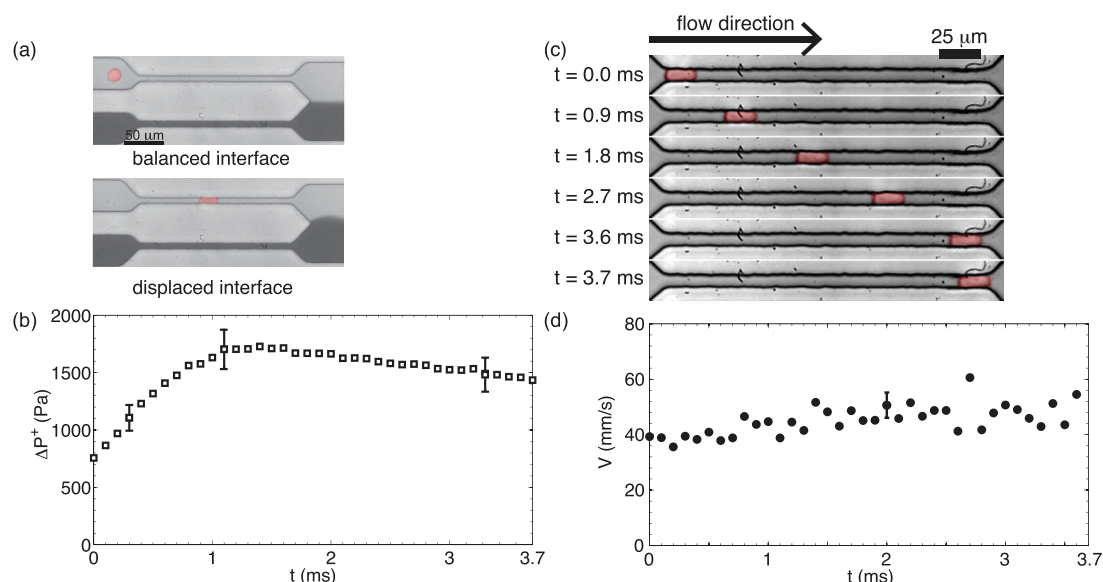


Figure 1. (a) Microfluidic device used to quantify cell passage time, cell velocity and excess pressure drop. Downstream of the constricted channels is a flow comparator to measure excess pressure drop of particles and cells. Upper panel: the driving pressures of the upper and lower channels are fixed such that the flow rates in the upper and lower streams are equal and the interface of the co-flowing streams is centered downstream when no particle is in the constriction. The interface is determined by fitting a sigmoid function to grayscale pixel values across the interface [8, 28]. Lower panel: a Jurkat leukemia cell is in the constriction and the interface between the co-flowing streams is displaced towards the blocked channel. Using a calibration relating the interface displacement to known excess pressures applied to the upper channel, the interface displacement can measure the excess pressure drop ΔP^+ . The uncertainty in determining ΔP^+ from an interface displacement calibration is approximately 10%. (b) ΔP^+ of a Jurkat leukemia cell (shown in (a)) while it is passing through the constriction. Given the uncertainty of 10%, ΔP^+ has reached a steady-state value during the passage time of the cell. (c) Passage of a Jurkat leukemia cell through a microfluidic constriction. Passage time τ_p is the time for an object to pass through the constricted channel once it has fully entered. (d) The velocity of the Jurkat leukemia cell while passing through the channel. The cell velocity is constant within the 10% measurement error and is not varying during the period that ΔP^+ has reached a steady-state. In all pictures the cell is highlighted in red.

with a concentration of 3×10^5 cells mL^{-1} , and brain cells with a concentration of 6×10^5 cells mL^{-1} .

Preparation of deformable particles

Elastic polydimethylsiloxane (PDMS) particles with different elastic moduli (G') were prepared by mixing PDMS pre-polymer and cross-linking agent (Sylgard 184, Dow Corning) with 60:1 and 30:1 ratios (corresponding to $G' = 2.5$ kPa and 95 kPa respectively). About 1 mL of the mixture was placed in a centrifuge tube with 5 mL of water containing 3 wt% Tween 80 surfactant, vigorously vortexed, and baked for 2 h at 80 °C. These particles with polydisperse sizes sediment under gravity and the smaller particles were harvested from the bottom of the centrifuge tube with a pipette. The elastic moduli of cured bulk samples were measured with an AR-2000 rheometer.

Emulsions were made by placing oil into a container with water and shaking the mixture by hand or using a vortex mixer. Interfacial tension was adjusted by varying the concentration of surfactants in water and hexadecane. Water containing either 0.02 wt% ($\gamma = 14$ mN m^{-1}) or 0.2 wt% Tween 20 surfactant ($\gamma = 7$ mN m^{-1}) [30] was used. For one sample both water and oil contained surfactants—0.2 wt% Tween 20 in water and 0.3 wt% Span 80 in hexadecane ($\gamma = 0.7$ mN m^{-1}) [30]. Silicone oil emulsions were prepared by emulsifying oils of known viscosity ($\mu_i = 5$ –97 000 $\text{mPa} \cdot \text{s}$)

with water containing 0.3 wt% of Tween 60 surfactant ($\gamma = 13$ mN m^{-1}) [31].

Microfluidic device design and fabrication

The devices consist of two parallel channels (40 μm wide, 500 μm long) tapering to constricted channels (channel lengths L , widths W and heights H are given in table 1 with reference to the samples used) as shown in figure 1. The constricted channels join a single wider channel (100 μm wide, 2 mm long) containing a flow-comparator based microfluidic manometer [8, 25–27]. The passage time and velocity is measured in the long constricted channels (figures 1(c) and (d)) and the excess pressure drop is determined from the microfluidic manometer (figure 1(b)). These three quantities are measured simultaneously.

Microfluidic devices were fabricated using standard soft lithography techniques [32]. Moulds were made by spin-coating SU8-5 negative photoresist (Microchem) on a 76.2 mm diameter silicon wafer. The thickness of the spin-coated layer corresponds to the height of the channels. PDMS was poured into the moulds, degassed, and baked for 2 h at 80 °C. The PDMS was cut, peeled from the mould, and inlet and outlet holes were punched (Harris Uni-core punches, 0.75 mm outer diameter). The devices were bonded to glass cover slides by exposing the surfaces to air plasma (Plasma Cleaner PDC-32G, Harrick Plasma), putting the devices and

Table 2. Dimensionless parameters and operating conditions of the study. $Re = \rho V_m 2R_h / \mu_o$ is the Reynolds number, $Ca = \mu_o V_m / \gamma$ is the capillary number, ρ is the suspending fluid density, μ_o is the viscosity of the suspending fluid, R_h is the hydraulic radius of the constricted channel, V_m is the undisturbed mean fluid velocity, σ is the shear stress, and γ is the interfacial or membrane tension. Cell membrane tensions were estimated to be $0.01\text{--}1\text{ mN m}^{-1}$ [33, 34]. For elastic particles $Ca \approx \mu_o V_m / G'R$, where G' is the particle's elastic modulus and R is the particle's radius.

Sample	Re	Ca	V_m (m s ⁻¹)	σ (Pa)	P_i (Pa)
LNCaP	0.49	0.071 – 7.1	0.053	4.6 – 6.2	7350
CL-1	0.49	0.071 – 7.1	0.053	2.2 – 5.1	7350
CL-2	0.49	0.071 – 7.1	0.053	3.0 – 5.5	7350
Jurkat	0.086 – 0.37	0.018 – 5.9	0.014, 0.044	0.38 – 1.2	2116, 6812
CCRF-CEM	0.37	0.059 – 5.9	0.044	3.1 – 9.0	6812
CCRF-CEM LatA	0.37	0.059 – 5.9	0.044	7.7 – 11	6812
A172	0.38	0.053 – 5.3	0.040	0.96 – 6.3	6550
1321N1	0.41	0.058 – 5.8	0.043	1.2 – 3.2	6550
Benign glial cells	0.41	0.058 – 5.8	0.043	2.0 – 3.3	6550
Hexadecane	0.12–0.37	0.0031 – 0.063	0.014, 0.044	0.21 – 9.8	2064, 6812
Silicone oil	0.37	0.0034	0.044	1.5 – 9.1	6812
PDMS	0.12–0.37	2.0×10^{-5} – 0.0045	0.014, 0.044	0.16 – 8.2	2064, 6812

glass into contact, and then baking at 80 °C for 4 min. All devices used with deformable particles were infused with water, and devices used with cells were infused with 0.01 M phosphate-buffered saline solution (PBS) to maintain hydrophilicity until use. Prior to experiments with adherent cells, the devices were incubated with a mixture of 4 wt% bovine serum albumin (BSA) in 0.01 M PBS for 1 h to reduce the adhesion of cells to the channel surfaces.

Microfluidic device operation

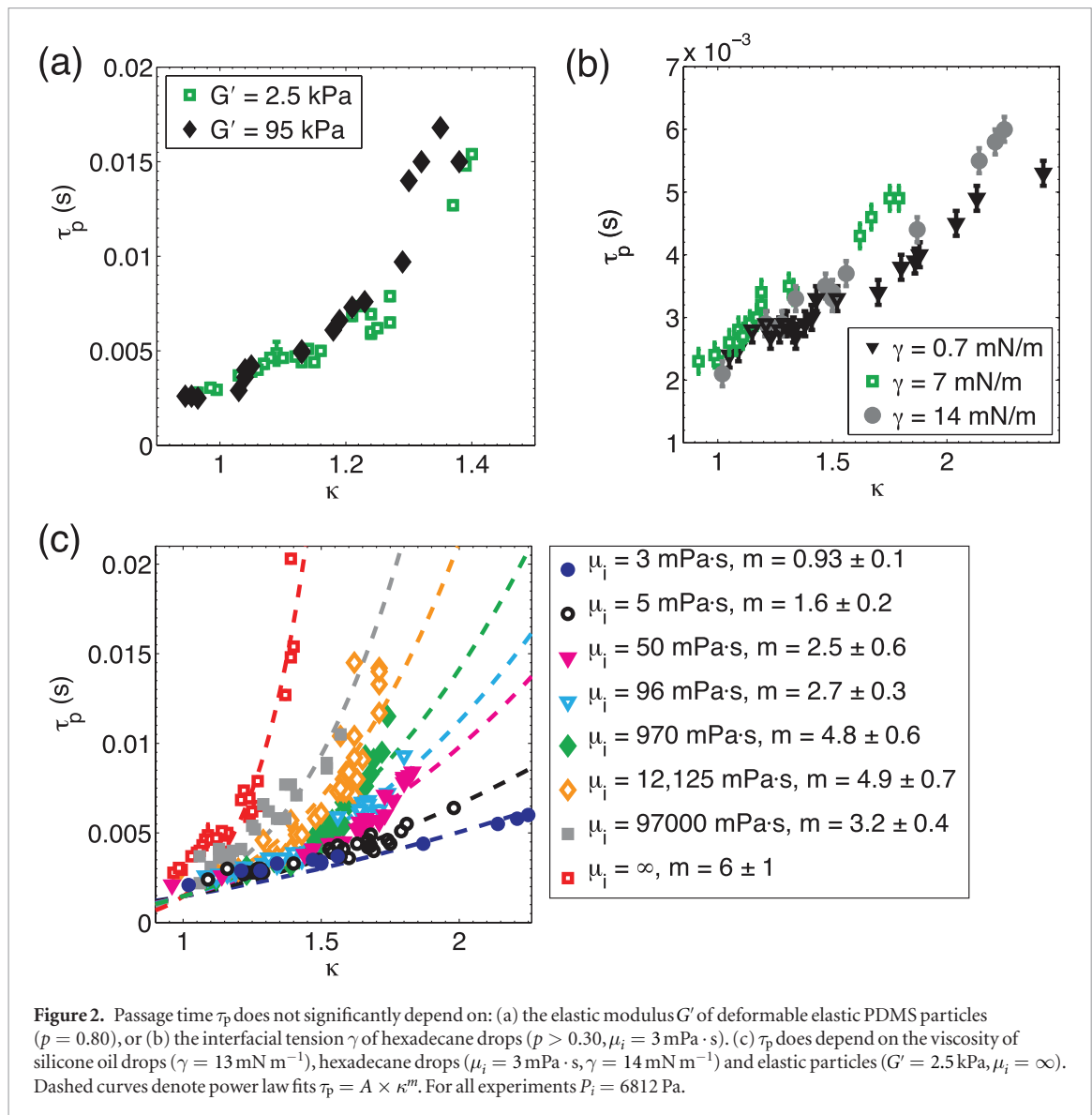
For cell experiments, growth medium containing cells and Trypan Blue dye (viscosity $1.34\text{ mPa} \cdot \text{s}$, density 1020 kg m^{-3} , Cellgro), and medium containing McCormick black food dye (viscosity $1.44\text{ mPa} \cdot \text{s}$, density 1100 kg m^{-3}) were loaded into two fluid reservoirs attached to vertically mounted optical rails (Edmund Optics). Black food dye was used to visualize the displacement of the interface between the two streams. The reservoirs were connected to the device inlets using 0.5 mm inner diameter tygon tubing, 20 gauge stainless steel blunt tips, and 20 gauge hollow blunt pins. The device outlet was left open to the atmosphere. The pressure drop associated with the tubing was 0.1% of the pressure drop in the chip. For deformable particle experiments the device operation was identical to that used for cells, except that in place of cells particles were loaded into one reservoir where the suspending fluid was deionized water (viscosity $1\text{ mPa} \cdot \text{s}$, density 1000 kg m^{-3}), while a mixture of water and McCormick black food dye (viscosity $1.44\text{ mPa} \cdot \text{s}$, density 1100 kg m^{-3}) was loaded into the other reservoir. A summary of the device operating parameters are given in table 2.

All experiments were conducted in bright-field mode using an Olympus IX-70 inverted microscope

equipped with a $40\times$ magnification objective and a Phantom v310 12-bit CMOS camera with $20\text{ }\mu\text{m}^2$ pixels. With this setup, the effective pixel size is $0.46\text{ }\mu\text{m}$. Typically frame rates ranging from 3000–10 000 frames per second and exposure times of 30 μs were used to observe the motion of objects passing through the constriction and interface displacements. Lower frame rates were used for lower driving pressures.

Passage time and velocity measurement

The passage time τ_p was measured from the images using ImageJ software, where τ_p is defined as the time for an object to transit through the constriction channel once it has fully entered and while it is still fully contained—see figure 1(c). Note that this definition does not include the entry time, i.e. the time it takes for the cell to enter the constriction channel, as has been considered in combination with the passage time in some previous studies [12, 13]. The uncertainty in τ_p was taken to be the time to obtain two images, as a particle may have passed into or out of the constriction between frames. Twenty particle sizes were obtained from elliptical fits to the edges of the particles prior to entry using ImageJ software or Matlab's image processing toolbox. The centroid of the particle was used to determine the instantaneous particle velocity. Since particles were not strongly confined, they were assumed to have an ellipsoid shape while in the constricted channel. The volume was calculated using the major and minor axes and the channel height. The radius R was determined from the volume for an unconfined sphere. The uncertainty in R , determined from the range of measured major and minor axes for each particle, is one-half of the pixel width ($0.23\text{ }\mu\text{m}$ at $40\times$). Particle confinement is defined as $\kappa = R/R_h$ where $R_h = (W \times H)/(W + H)$ is the hydraulic radius of the constricted channel.



Excess pressure drop measurement using the microfluidic manometer

Figure 1(b) shows our approach for measuring the excess pressure drop ΔP^+ of particles and cells using a microfluidic manometer [8, 25]. This method is based on a flow-comparator principle where the displacement of a co-flowing laminar interface is directly related to ΔP^+ via a ΔP^+ -interface displacement calibration [8]; see figure 1(b) for a typical ΔP^+ profile. The ΔP^+ signal increases when a cell enters the constriction, reaches a peak, and then declines as the cell moves away from the constriction. The response time of the manometer is set by the longest timescale associated with fluid interface displacements [25, 27]. In our experiments the longest timescale is for interface motion, $t_I \approx W_D/2V_m \approx 1 \text{ ms}$ for the data shown in figure 1, where W_D is the width of the downstream channel and V_m is the unperturbed mean velocity of the fluid. Beyond this longest timescale, in figure 1(b), we show that the cell response has reached a steady state (within the 10% measurement error [8]) and can be characterized by the peak in the ΔP^+ signal. Figure 1(d) shows that the cell

velocity is nearly constant during the steady state period of ΔP^+ . The cell shape or length does not change once it has fully entered the channel.

Results

Passage times of deformable particles depend on particle size and viscosity

Given the complexity of cells and cell-surface interactions, we sought to clarify which mechanical properties influence τ_p . We measured the passage times of synthetic particles whose mechanical properties (elastic modulus G' , interfacial tension γ , and viscosity μ_i) were independently varied, in a similar manner as previous studies of cell deformability in microfluidic devices [4, 35].

The passage time for both the elastic particles and viscous drops increases with particle size (or confinement κ) as shown in figure 2. We observe that varying the elastic modulus of PDMS particles by 38 times does not significantly alter the dependence of τ_p on confinement κ , as shown in figure 2(a). Likewise τ_p does not

strongly depend on the interfacial tension of viscous hexadecane drops, where γ was varied by a factor of 20 by adding surfactants to the suspending fluid ($\gamma = 7$ and 14 mN m^{-1}) and oil phases ($\gamma = 0.7 \text{ mN m}^{-1}$) (figure 2(b)). There appears to be a weak non-monotonic dependence of τ_p on γ , similar to that observed for air bubbles suspended in fluids containing surfactants [36]. We find that τ_p strongly depends on drop viscosity as shown in figure 2(c) where viscosity is varied by a factor of 32 000. We also contrast τ_p for elastic particles ($\mu_i = \infty$) and viscous drops in figure 2(c), and find that τ_p for elastic particles is larger than the highest drop viscosity tested. For both viscous drops and elastic particles, the dependence of τ_p on κ is well-described by power law fits (dashed curves) [9, 24]. For viscous drops the power law exponent increases with increasing viscosity as $\tau_p \approx 0.0015 \times \kappa^{1.9(\mu_i/\mu_o)^{0.076}}$.

Particle viscosity affects friction and lubrication film thickness

Figure 2 suggests that in terms of mechanical properties, particle viscosity dominates the passage time at short timescales ($\sim 1\text{--}10 \text{ ms}$). This finding counters some prior notions on the role of the elastic modulus and viscosity on the passage of cells through microchannels. It has been argued that differences in the elasticity of the cell membrane or cytoplasm alone can explain differences in cell transit velocities and passage times, as cells with lower elastic moduli push less strongly against channel walls and experience weaker friction forces [9, 11, 13, 17]. This argument was made on the assumption that Newtonian liquid drops with the same interfacial tension would have the same lubrication film thickness, velocities, and passage times regardless of any difference in viscosities [11]—implying that drop viscosity does not impact the friction force. Our data in figure 2 shows that at least for short timescales, passage times (and therefore transit velocities) depend on the viscosity of Newtonian liquid drops. In this section, we conduct a force balance analysis on drops moving with a constant velocity and examine whether the drop viscosity also affects the friction force and lubrication film thickness at short timescales. We note that for the experiments reported here, the driving pressure is 6812 Pa and the capillary numbers corresponding to drops and elastic particles are $\text{Ca} \approx 10^{-3}\text{--}10^{-1}$ and $\text{Ca} \approx 10^{-5}\text{--}10^{-3}$ respectively (see table 2). Here the capillary number for drops is defined as $\text{Ca} = \mu_o V_m / \gamma$ where μ_o is the viscosity of the suspending fluid, V_m is the undisturbed mean fluid velocity, and γ is the interfacial tension. For elastic particles $\text{Ca} \approx \mu_o V_m / G'R$, where G' is the particle's elastic modulus and R is the particle's radius.

The macroscopic force balance on a particle moving with a constant velocity yields

$$F_p = F_{fr}, \quad (1)$$

where the pressure force F_p driving the drop is balanced by the hydrodynamic friction force F_{fr} . Given that

equation (1) is valid when the particle is not accelerating, we sought to identify the conditions under which the different particles used in our study were moving with a steady velocity. Figure 3 shows the deviation from the mean velocity ($\langle V \rangle$) for representative viscous drops and elastic particles with three different confinement values. For $\kappa \approx 1.0$, both the viscous drops and elastic particles deviate less than 10% from the mean velocity. Similar levels of deviation are observed for moderately confined ($\kappa \leq 1.5$) drops with viscosity $\mu_i \leq 970 \text{ mPa} \cdot \text{s}$ (see figures 3(a)–(c)). Given that our measurement error in V is $\approx 10\%$, most of the systems we studied therefore have a nearly constant velocity. However, strongly confined drops with $\mu_i \geq 970 \text{ mPa} \cdot \text{s}$ and elastic particles have large velocity fluctuations which may result from slight deviations in channel width, as well as a rather thin lubricating layer of the suspending fluid.

For particles which move with a constant velocity, the friction force experienced by the particle is a function of its confinement, as shown in figure 4(a). Here we calculate the friction force from equation (1) by recognizing that

$$F_p = \Delta P_M^+ S_{cs} \quad (2)$$

where ΔP_M^+ is the peak excess pressure drop directly measured with a microfluidic manometer (see the materials and methods, and figure 1) and $S_{cs} \approx \pi R_h^2$ is the cross-sectional area of the particle [18]. We find that the friction force increases with drop viscosity as well as particle confinement, but the friction force on a particle does not seem to change strongly when its elastic modulus is varied (figure 4(a)).

To estimate the lubrication film thickness, we assume that most of the dissipation due to motion against the channel walls arises from shearing a thin film of the suspending fluid. A Couette flow is expected to occur in the film if the viscous stress in the lubricant is lower than would be in the particle without a lubricating layer. This condition can be expressed as $(\mu_i/R)/(\mu_o/\delta) \gg 1$ where R ($\approx R_h$) is the particle radius in the constricted channel and δ is the average thickness of the lubricating film given that the film is non-uniform in our microchannels [18, 37]. For Couette flow, the friction force is given by:

$$F_{fr} = \mu_o V S_{ct} / \delta, \quad (3)$$

where $S_{ct} \approx 2\pi R_h L_p$ is the surface area of the particle in contact with the lubricating film [18, 37] and L_p is the particle length. By measuring L_p and using equations (1)–(3), we calculate δ . As shown in figure 4(b), we find that the average film thickness decreases with increasing particle confinement and viscosity. Using our estimates of lubrication film thickness, we also find that the assumed Couette flow criterion is valid for elastic particles ($\mu_i = \infty$) and drops with viscosities ranging from 970–97 000 $\text{mPa} \cdot \text{s}$. Thus, for the flow conditions tested here, $\text{Ca} \approx 10^{-3}\text{--}10^{-1}$, the friction force and lubrication film thickness

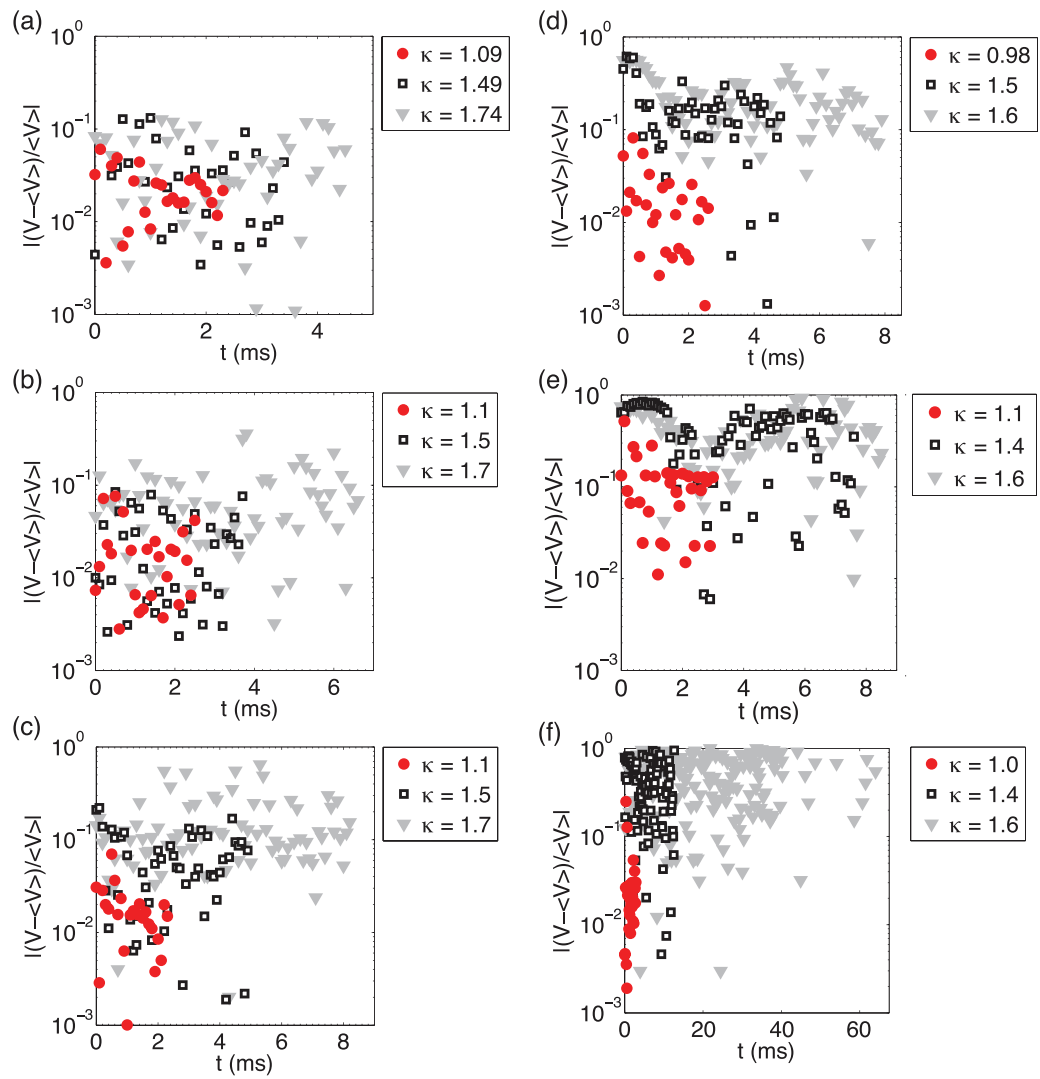


Figure 3. Normalized deviations from the mean velocity $|V - \langle V \rangle| / \langle V \rangle$ plotted against time t for: (a) $5 \text{ mPa} \cdot \text{s}$, (b) $96 \text{ mPa} \cdot \text{s}$, (c) $970 \text{ mPa} \cdot \text{s}$, (d) $12\,125 \text{ mPa} \cdot \text{s}$, and (e) $97\,000 \text{ mPa} \cdot \text{s}$ oil drops, as well as (f) elastic particles with $G' = 2.5 \text{ kPa}$. Time $t = 0$ corresponds to the time when the particle has first fully entered the constricted channel. This shows that V of weakly confined drops does not deviate strongly from $\langle V \rangle$. For all experiments $P_i = 6812 \text{ Pa}$.

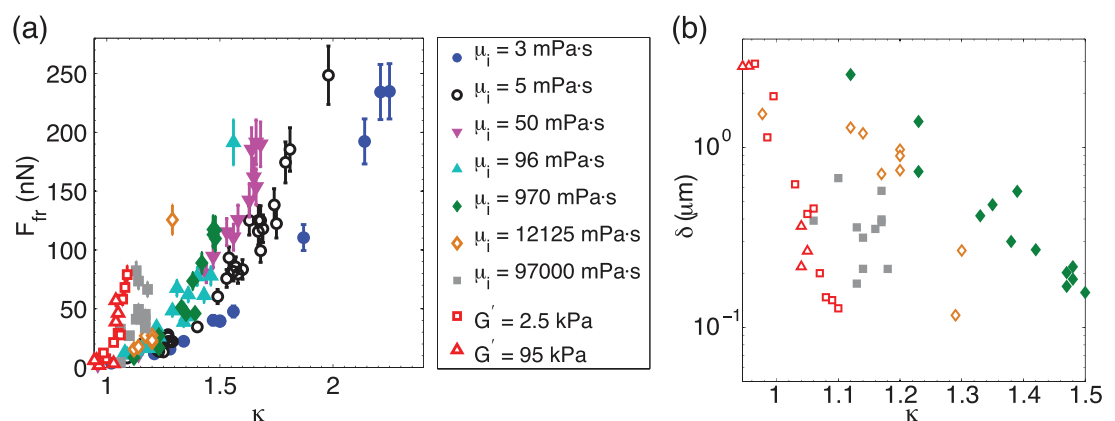


Figure 4. (a) Friction force depends on particle confinement and increases with drop viscosity. The data is shown for drops and elastic particles moving with nearly constant velocity ($P_i = 6812 \text{ Pa}$). (b) Estimated lubrication layer thickness δ depends on confinement κ for the same particles shown in (a). See text for details.

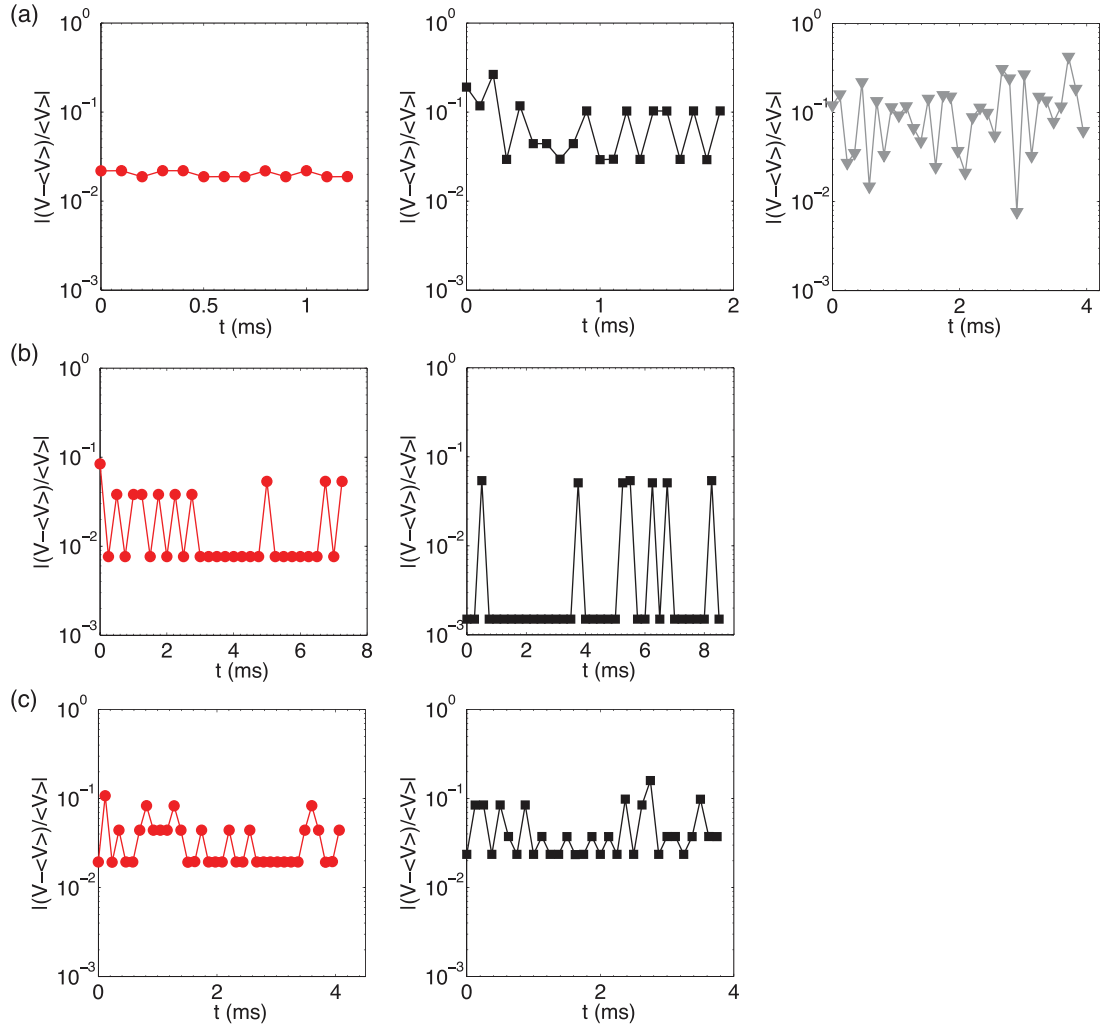


Figure 5. Normalized deviations from the mean velocity $|V - \langle V \rangle|/\langle V \rangle$ plotted against time t for: (a) a CCRF-CEM leukemia cell with confinement $\kappa = 1.1$ (left), $\kappa = 1.4$ (center), and $\kappa = 1.6$ (right). $P_i = 6812$ Pa. (b) A CL-2 prostate cancer cell with $\kappa = 1.1$ (left) and $\kappa = 1.4$ (right). $P_i = 7350$ Pa. (c) A A172 glioblastoma cell with $\kappa = 1.1$ and $\kappa = 1.5$. $P_i = 6550$ Pa. Time $t = 0$ corresponds to the time when the cell has first fully entered the constricted channel. The line connecting neighbouring points in all graphs is a guide for the eye. This shows that V of cells with $\kappa \leq 1.4$ does not deviate strongly from $\langle V \rangle$.

depend on drop viscosity and confinement. Strikingly for $\text{Ca} \approx 10^{-5}$ – 10^{-3} , the elastic modulus of a confined particle does not influence the friction force or lubrication film thickness.

Cell friction forces and lubrication film thickness

We pursued a similar force balance analysis with cells as we did for deformable particles. Figure 5 shows that all three types of cells (leukemia, prostate, and brain) move with a nearly constant velocity, justifying the use of the force balance prescribed by equation (1). Figure 6 shows the friction force and film thickness as a function of confinement. We find that with increasing confinement, friction forces generally increase while film thicknesses decrease.

Figure 6 shows that the relative values of our estimated film thickness for cells are $\delta/R_h \approx 0.01$ – 1 for a confinement of $1 < \kappa < 1.4$. Taking the nominal radius of the microchannels as $R_h \approx 10 \mu\text{m}$ (exact values are provided in table 1), we obtain film thickness ranging from 0.1 – $10 \mu\text{m}$. The larger film thickness values of

1 – $10 \mu\text{m}$ are obtained for smaller cells ($1 < \kappa < 1.2$), where the confined cell shape is far from rod-like and the lubricating films are not well defined. In contrast, for more confined cells ($1.2 < \kappa < 1.4$), lubricating films are well developed and we estimate film thicknesses ranging from 0.1 – $1 \mu\text{m}$. It is important to mention that due to the rectilinear cross-section, planar lubricating films exist on channel walls, but gutters occur at the corners. As a result, our estimates of film thickness (based on equation (3)) represent average values of the lubricating layer profile in the microchannel.

Given that for the more confined cells, the calculated film thickness is in the range of 0.06 – $1 \mu\text{m}$, we suggest that our operating conditions pertain to the hydrodynamic friction regime and that surface forces do not affect cell passage times. Using reflectance interference contrast microscopy, Preira *et al* measured the planar film thickness to be $\approx 70 \text{ nm}$ for cell velocities in the range of 100 – $1000 \mu\text{m s}^{-1}$ and indicated that surface forces can affect cell velocity [18]. Since our cell velocities are an order of magnitude higher than Preira *et al*,

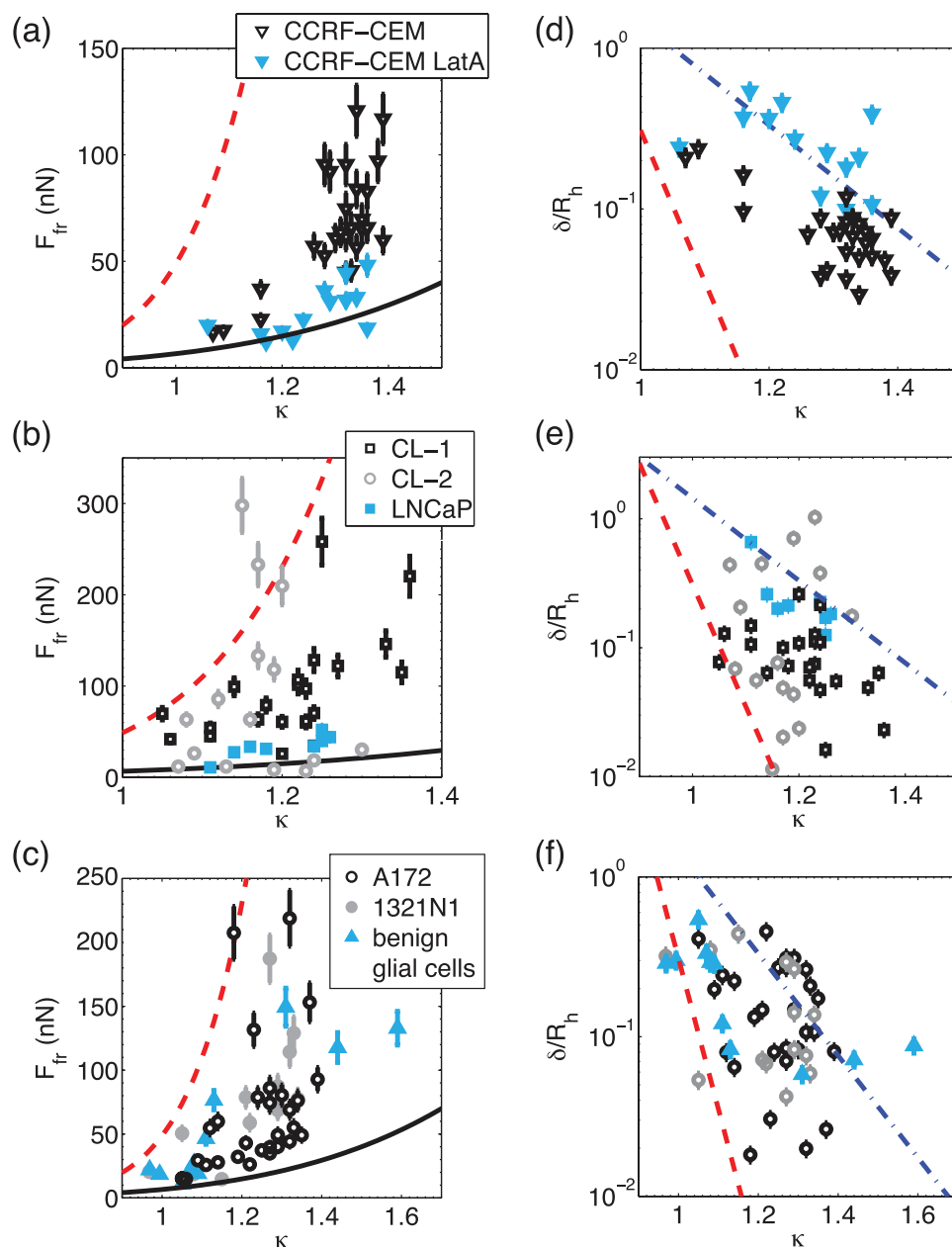


Figure 6. Friction force and lubrication film thickness produced by ((a) and (b)) leukemia cells ((c) and (d)) prostate cancer cells and ((e) and (f)) brain cells. The red and black curves in ((a)–(c)) denote the fit curves for elastic particles and the lowest drop viscosity respectively. In ((d)–(f)) the red dashed curves are the normalized film thickness for elastic particles and the blue dash-dot curves are for 970 mPa · s drops. This is the lowest viscosity (of the data we have) where we expect a Couette flow to occur in the lubrication film. The curves were obtained from exponential fits to the film thickness versus confinement data ($R^2 \geq 0.93$). $P_i = 6550$ – 7350 Pa.

it is reasonable to expect larger film thicknesses. Thus, for millisecond deformation timescales, our results indicate that cell passage time is determined by the hydrodynamic shear stress in the lubricating film and not by surface interactions with the wall.

In figure 6, the friction force for cells lies within the bounds delineated by the friction curves of elastic particles and the lowest drop viscosity (3 mPa · s) with most of the cancer cell data being closer to the drop measurements than elastic particles. In addition, the film thickness values for the cells tend to be larger than the curve bounded by the elastic particles and fall in the same range as drops. Both these findings suggest that in the hydrodynamic friction regime, the transport

characteristics of cancer cells are closer to those of viscous drops than elastic particles.

Influence of driving pressure on passage time and friction force

Our results indicate that particle viscosity and confinement affect passage time, friction force and lubrication film thickness. These results were obtained from experiments conducted at a driving pressure of $P_i \approx 7000$ Pa. We asked whether these results would also hold for a lower driving pressure. The lowest driving pressure that we could test in our setup was $P_i \approx 2000$ Pa, below which diffusional smearing of the interface in the microfluidic manometer was substantial.

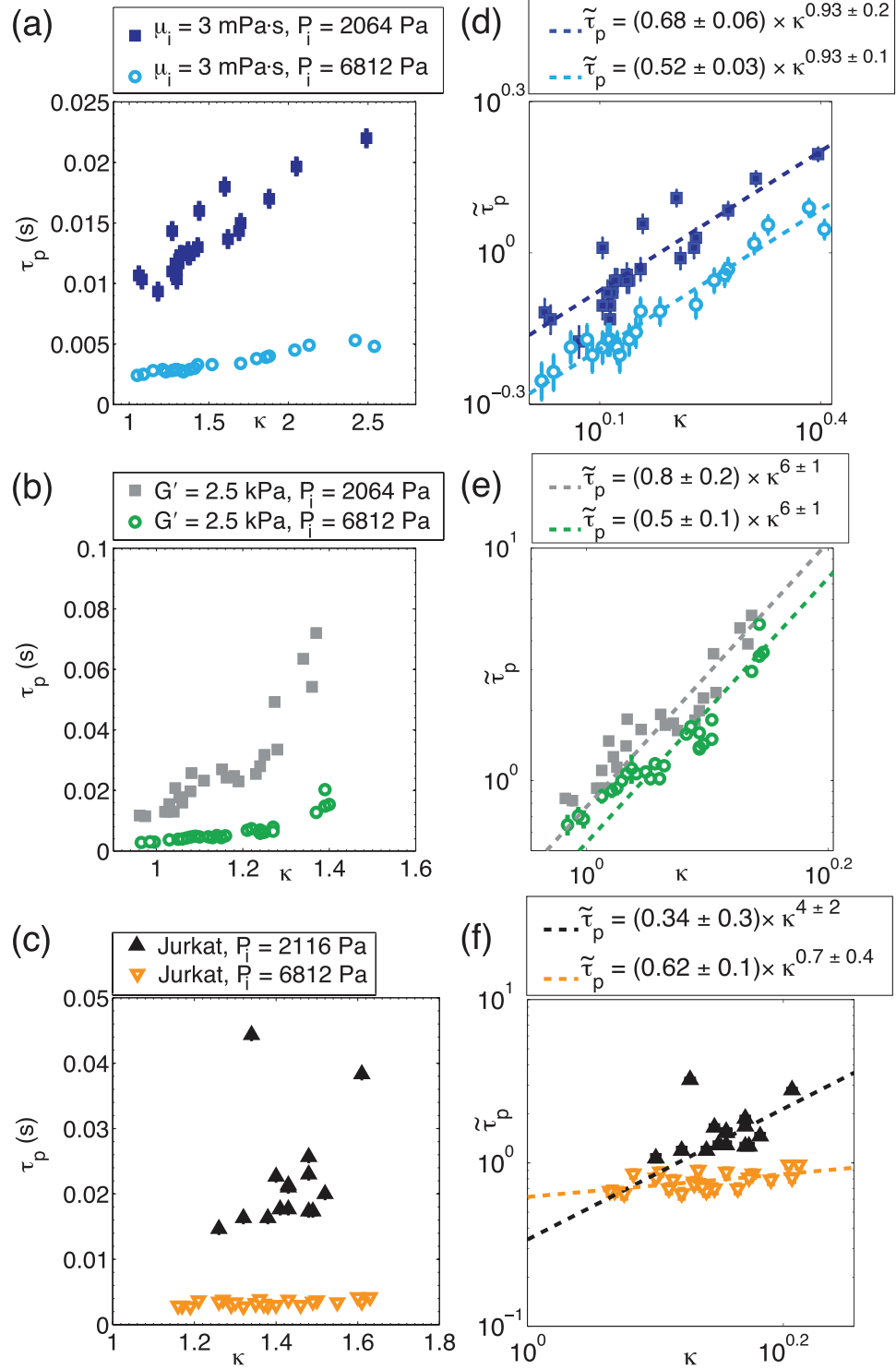


Figure 7. Passage times τ_p obtained at lower driving pressures P_i are larger for (a) viscous hexadecane drops, (b) elastic particles, and (c) Jurkat leukemia cells ($n = 16$ for $P_i = 2116$ Pa, $n = 24$ for $P_i = 2116$ Pa). Nondimensional passage times $\tilde{\tau}_p = \tau_p V_m / L_{CH}$ are significantly different at different P_i for (d) hexadecane drops ($p = 0.0041$), (e) elastic particles ($p = 0.040$), and (f) Jurkat cells ($p = 2.0 \times 10^{-7}$). Note the logarithmic axes in (d)–(f). Dashed lines denote power law fits $\tilde{\tau}_p = A \times \kappa^m$.

Figure 7 compares the passage time data at high and low driving pressures for viscous drops (figure 7(a)), elastic particles (figure 7(b)), and Jurkat leukemia cells (figure 7(c)). In all cases τ_p was larger for lower P_i because the fluid velocity pushing the particle through the channel was lower. To account for the different fluid velocities (due to different P_i) τ_p was nondimensionalized as $\tilde{\tau}_p = \tau_p V_m / L_{CH}$, where V_m is the mean

undisturbed fluid velocity (i.e. in the absence of the particle). We note that this nondimensionalized passage time can also be viewed as the inverse of particle mobility defined as the ratio of the mean fluid velocity to the transit velocity of the particle, i.e. $\tilde{\tau}_p = V_m / V$. We observe that this nondimensionalization brings the data sets closer together but does not collapse the data for particles or cells (figures 7(d)–(f)).

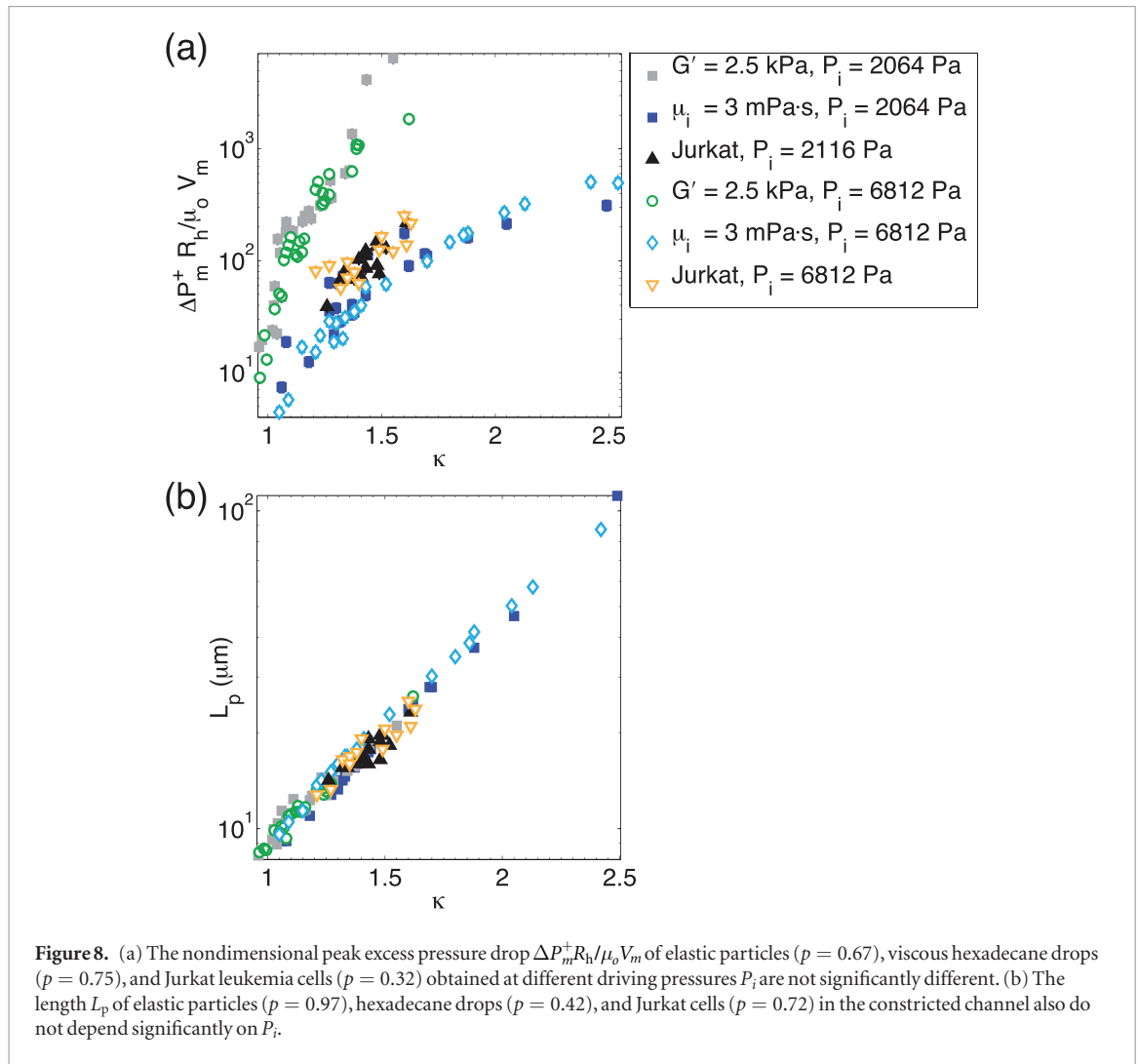


Figure 2(c) shows that drop passage time data fit the power law $\tilde{\tau}_p = A \times \kappa^m$, where m captures the drop viscosity dependence. We apply the same power law fit to the data in figure 7 and find that the viscosity-dependent power m does not change for drops and particles at different P_i . Instead, for both drops and elastic particles, A decreases with increasing P_i . This suggests that, in the power law $\tilde{\tau}_p = A \times \kappa^m$, A and m encode driving pressure and viscosity dependence respectively. Therefore if drops with other viscosities or particles with different elastic moduli were also tested at lower driving pressures the trends would be the same as in figure 2(c). Thus, viscosity and not elastic modulus affects passage time even at this lower driving pressure.

In contrast to the deformable particles, the passage time of cells for the low and high driving pressure show different functional dependence with size despite the nondimensionalization (figure 7(f)), i.e. the exponent m (from fits $\tilde{\tau}_p = A \times \kappa^m$) decreases with increasing P_i . This can occur if the cell rheological properties change at different flow velocities or shear rates; for example, Tsai *et al* modelled neutrophils entering into a micro-pipette as shear thinning fluids [38]. The power law multiplicative factor A also changes under different driving pressure conditions (figure 7(f)). Thus,

although the passage time for both the deformable particles and cells can be fit to power laws, the viscosity-dependent exponent m and driving pressure-dependent prefactor A are very different, and the empirical expression relating passage time to confinement for drops does not fit the cell data.

Differences in $\tilde{\tau}_p$ for different P_i can occur if the friction force F_{fr} experienced by particles and cells is higher at low P_i , and does not scale linearly with the mean fluid velocity. Considering that F_{fr} is balanced by the pressure force F_p for sufficiently small confinements κ , we examined if the peak excess pressure drop ΔP_m^+ scales with V_m by nondimensionalizing it as $\Delta P_m^+ R_h / \mu_o V_m$ [39]. We find that the nondimensional peak excess pressure drop for different P_i is not significantly different for elastic particles, drops, and cells over our entire range of κ (figure 8(a)); therefore differences in the pressure force for different P_i do not account for differences in $\tilde{\tau}_p$. The particle length L_p while in the constricted channel and lubrication layer thickness δ both contribute to F_{fr} for highly viscous objects like cells [18]. It is possible that L_p depends on P_i . We found that differences in L_p for particles, drops, and cells at different P_i are not significant within the accuracy of our measurement (figure 8(b)). We conclude that the lubrication layer thickness δ is

reduced at a lower P_i and does not scale linearly with V_m , resulting in a higher $\bar{\tau}_p$ which contributes to changes in the power law multiplicative factor A .

Discussion

Role of particle rheology and friction on passage time

The passage time and friction force for emulsion droplets of varying viscosity, elastic particles of different elastic modulus, and cells are found to be in the hydrodynamic friction regime. Passage time, friction force, and lubrication film thickness vary with the droplet viscosity, but not with the particle elastic modulus. The friction force and lubrication film thickness data for different cancer cells lie within the range of viscous drop measurements rather than that of elastic particles. A potential explanation for this viscous response is that in the hydrodynamic friction regime, the membrane of the cancer cell is similar to that of the drop's viscous interface rather than the rigid interface of a solid elastic particle. Typical cells are bounded by a ~ 5 nm thick plasma membrane, which is tethered to a 200–500 nm thick actomyosin cortex by transmembrane proteins. The actomyosin cortex has been previously modeled as a viscoelastic gel-like fluid which flows under mechanical perturbations [40].

Although the Couette flow model for the lubrication layer (equation (3)) does not incorporate the viscosity contrast across the drop interface, it is possible that the viscosity dependence of the lubrication layer thickness can be found by including a tangential stress boundary condition that couples the drop and suspending fluid viscosities. It is also possible that the scatter observed for cancer cells within the two bounding curves in figure 6 is associated with different degrees of viscous resistance offered by the membrane or intracellular fluid of individual cells. Further studies are needed to verify these hypotheses.

Our findings are in contrast with the prior notion that elasticity affects the passage time of cells [9, 11, 13, 17]. Given that passage times and cell velocities in previous studies vary by five orders of magnitude, it is possible that differences in elastic modulus and not viscosity can affect passage times for different driving and confinement conditions than those considered here [10–12], since our study focused on a narrow driving pressure range (see table 2). Different regimes can be expected depending on the operating conditions, such as those reported in tribology studies [41, 42]—(i) A hydrodynamic lubrication regime, where fluid stresses control the particle velocity, lubrication film thickness and friction forces. Such a regime can be expected at high particle velocities, where the lubrication film thickness is larger and the hydrodynamic friction forces dominate. (ii) A boundary lubrication regime, where the surface interactions between the particle and channel wall control particle behavior and friction. In this case, the normal stresses exerted by the confined particle can

cause very thin lubricating films promoting surface and intermolecular interactions and wall roughness can play a major role. Such a situation is expected at low particle velocities and with strong confinement. (iii) Finally, a mixed lubrication regime can also occur where both hydrodynamic and surface forces can be important in regulating particle motion and friction.

The existence of these different friction regimes, coupled with the excitation-dependent rheology of cells, makes inference of cell mechanical properties from passage time alone difficult. Nevertheless, our study shows that a regime exists where passage time encodes the viscous response of cells. Implementation of microfluidic manometry, direct measurement of the thickness of the lubricating layer, as well as the use of synthetic deformable particles (including vesicles [43] and hydrogel particles [44, 45]) over a wider range of operating conditions than explored here, should provide considerable insight into this problem.

Significance of passage time as a metric for invasive potential of cancer cells

Several studies have used passage time (or transit velocity) to infer the invasive potential of cancer cells as it is a simple metric. Some of these studies have produced conflicting results, even when the same set of cell lines were chosen. Although our studies have not been designed to resolve this conflict, in this section we discuss this prior work and comment on the implications of our findings on connecting passage time to the invasive potential of tumor cells.

Hou *et al* ($\tau_p \approx 0.5$ –1 s, $L_{CH} = 150$ μm , $V \approx 150$ –300 $\mu\text{m s}^{-1}$) found that transit speeds and passage times of breast cancer (MCF-7) and benign breast (MCF-10A) epithelial cells were similar [7], whereas Guan *et al* ($\tau_p \approx 100$ –1000 s, $L_{CH} \approx 115$ μm , $V \approx 0.12$ –1.2 $\mu\text{m s}^{-1}$) demonstrated that it was possible to distinguish these same cell lines using passage time—though their definition of passage time included the time for the cell to enter the channel [12]. Byun *et al* [9] ($\tau_p \approx 10$ ms–10 s, $L_{CH} = 50$ μm , $V \approx 5$ –5000 $\mu\text{m s}^{-1}$) showed that cell passage times depend on cell mass, frictional interactions between the cells and channel (by immobilizing positive charges on the channel walls), and cell deformability (using an F-actin depolymerizing treatment). They found differences in passage times of human (highly invasive H1975 and less invasive HCC827) and mouse lung cancer cells (TMet, TnonMet, and TMet-Nkx2-1), with passage times being shorter for invasive cells. Additional studies that have investigated passage time include that by Gabriele *et al* ($\tau_p \approx 1$ –100 s, $L_{CH} = 2250$ μm , $V \approx 23$ –2300 $\mu\text{m s}^{-1}$) [11], Adamo *et al* ($\tau_p \approx 1$ –10 ms, $L_{CH} = 15$ μm , $V \approx 5000$ –100 000 $\mu\text{m s}^{-1}$) [13], and Ji *et al* ($\tau_p \approx 20$ –160 ms, $L_{CH} = 200$ μm , $V \approx 1250$ –10 000 $\mu\text{m s}^{-1}$) [15], but these investigations do not focus on metastatic potential differences between tumor cells; however, the cited works collectively highlight the five orders of magnitude variations in passage times and cell velocities reported in literature.

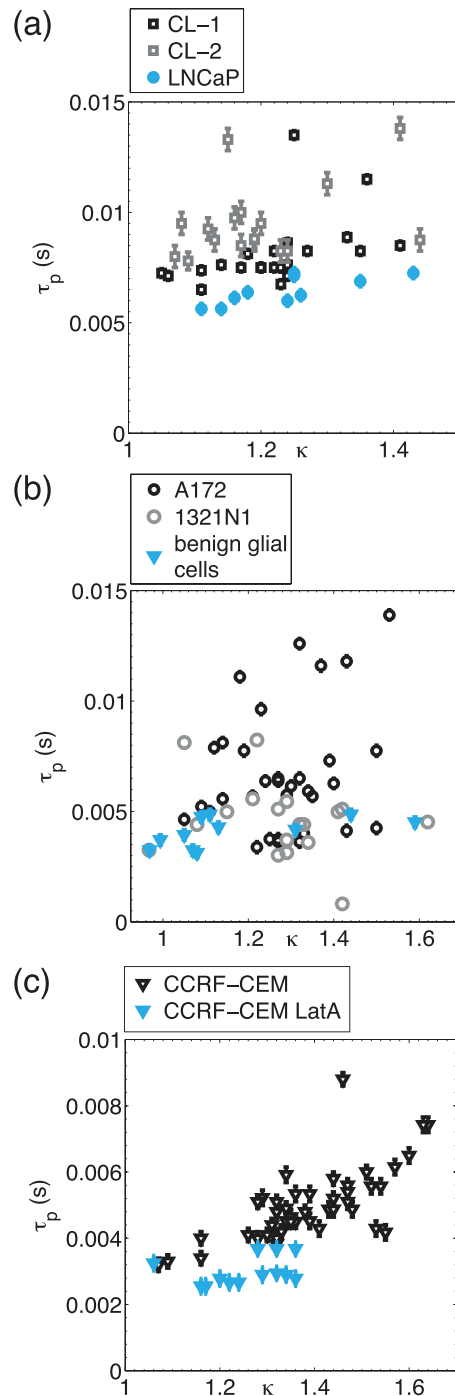


Figure 9. τ_p can be used to distinguish some cells with different physiological conditions. (a) τ_p of highly aggressive CL-1 ($n = 23$) and CL-2 ($n = 18$) prostate cancer cells are significantly larger than for less aggressive LNCaP ($n = 10$) prostate cancer cells ($p < 1.4 \times 10^{-4}$ with a two-sample Kolmogorov-Smirnov test, $P_i = 7350$ Pa). (b) τ_p of highly aggressive A172 glioblastoma ($n = 34$) and aggressive 1321N1 astrocytoma ($n = 18$) are not significantly different from benign glial cells ($n = 11$, $p > 0.090$, $P_i = 6550$ Pa). τ_p increases with increasing confinement κ as expected [24], and this increase is lower for lowly aggressive cells. (c) τ_p of CCRF-CEM leukemia cells treated with the F-actin depolymerizing drug Latrunculin A (LatA, $n = 13$) are significantly smaller than for control cells ($n = 45$, $p = 1.7 \times 10^{-6}$, $P_i = 6812$ Pa). Chips used with adherent prostate and brain cells were pre-treated with bovine serum albumin (4 wt% for 1 h) to reduce non-specific cell adhesion [7].

Our study shows that the τ_p for highly invasive prostate cancer cell lines CL-1 and CL-2 is significantly larger than for lowly invasive LNCaP prostate cancer cells (see figure 9(a)). However, differences in τ_p among highly invasive A172 glioblastoma, invasive 1321N1 astrocytoma, and benign glial cells are not statistically significant ($p > 0.05$, figure 9(b)). Note that variations in τ_p can be large and more pronounced for highly aggressive than for lowly aggressive or benign cells. This could be due to inherent variation in metastatic potential originating from changes in actin network structure [46–48], nuclear structure [4, 49, 50], or glycocalyx surface molecule expression [9, 51].

Prior work and our results with different cancer cells lines reveals that passage time is not necessarily a universal mechanical metric for malignancy, potentially due to the diversity in cancers. Similar conclusion was reached by measurement of adherent cell rheology of various cells lines, using magnetic twisting cytometry [52]. However, interestingly, when Hou *et al* [7] and Guan *et al* [12] tested the same set of breast cancer cells, different results were produced. Given the wide range of deformation timescales used in the studies, the rheological response of the cell may vary, giving rise to conflicting findings. Rheometric methods (e.g. AFM) have shown that for timescales greater than 1 s, the cytoskeleton dominates cell deformation that is described by power law rheology [19, 53]. For timescales much smaller than 1 s, cell mechanics is dominated by intracellular fluid flow [20]. This general picture is accepted for adherent cells; however it remains to be fully explored whether a similar description holds for suspended cells [54] commonly used in microfluidic cell deformability investigations. In fact, our observation of highly invasive prostate tumor cells being ‘less deformable’ (i.e. having longer passage times) than lowly invasive cells is in contradiction with the prevailing notion from long timescale adherent cell rheology that invasive tumor cells are more deformable [9, 12, 46, 55–62], although exceptions do appear to exist [52, 63–65].

The importance of deformation timescales on cell rheology is further illustrated by our data in figure 9(c), where we show that lantrunculin A treated leukemia cells have lower passage times than control cells. The reduction in τ_p due to depolymerizing F-actin in cells has been previously observed [9, 11, 13, 15] and interpreted as being due to a reduction in cell elastic modulus, where treated cells exert weaker normal forces on channel walls than untreated cells and experience lower friction forces. Considering that with our P_i and κ conditions the elastic modulus does not significantly influence τ_p , the lower τ_p in our experiments can be equally explained by a reduction in the cytoplasm viscosity, since F-actin depolymerization decreases cell cytoplasm viscosity [66], though directly relating τ_p to cytoplasm viscosity is not straightforward.

Thus, relating passage times to cancer cell invasive potential can be difficult if deformation timescales are not taken into account in microfluidic studies. Likewise, the frictional interactions between cells and channel walls also needs to be taken into account with suitable channel wall coatings and friction force measurements. Future work needs to focus on measuring passage time (or transit velocity) and cell friction across a wide range of deformation timescales in various organ-specific cell lines whose metastatic potential has been well characterized.

Conclusions

At millisecond timescales, we show that the passage time and friction do not strongly depend on the interfacial tension or elasticity of deformable particles. Rather, they depend on the viscosity of the deformable particles. As a result, the rheological parameter that controls the transport of cells through narrow channels has a viscous origin at these timescales. Moreover, the film thickness at high cell velocities is found to be ≥ 100 nm, indicating our experimental conditions pertain to the hydrodynamic friction regime. These findings are relevant for microfluidic cell deformability studies that seek to achieve high throughput, inevitably forcing the cells at high velocities with short passage times.

A limited set of experiments exploring the influence of driving pressure show that the excess pressure drop (i.e. friction force) scales with the applied driving pressure, whereas particle length does not vary with changes in driving pressure. Importantly, the lubrication film thickness appears not to scale linearly with driving pressure, making it difficult to collapse nondimensionalized cell passage times obtained at different driving pressures. Given that cell passage times vary by five orders of magnitude in the literature, comparing passage time data from different studies and inferring cell response is not meaningful due to the different driving pressure conditions used in these studies. Finally, we emphasize that a deeper understanding of the confined flow of cancer cells in microfluidic capillaries warrants systematic identification of hydrodynamic, mixed, and boundary lubrication regimes, and how cell rheology changes in these regimes. This knowledge will help to elucidate the connection between passage times and cancer cell invasiveness.

Acknowledgments

This work was partially supported by the Cancer Prevention and Research Institute of Texas (Grant Nos: RP100680 and RP140298) and the American Brain Tumor Association. NK and SAV were additionally supported by the National Science Foundation CAREER: Grant No. 1150836. We wish to thank B Butler, D Maldonado, D E Solomon, S Sennoune, R Martinez-Zaguilan and P Syapin for experimental support.

References

- [1] Wirtz D, Konstantopoulos K and Searson P C 2011 The physics of cancer: the role of physical interactions and mechanical forces in metastasis *Nat. Rev. Cancer* **11** 512–22
- [2] Chambers A F, Groom A C and MacDonald I C 2002 Dissemination and growth of cancer cells in metastatic sites *Nat. Rev. Cancer* **2** 563–72
- [3] Kienast Y, von Baumgarten L, Fuhrmann M, Klinkert W E, Goldbrunner R, Herms J and Winkler F 2009 Real-time imaging reveals the single steps of brain metastasis formation *Nat. Med.* **16** 116–22
- [4] Gossett D R, Henry T K, Lee S A, Ying Y, Lindgren A G, Yang O O, Rao J, Clark A T and DiCarlo D 2012 Hydrodynamic stretching of single cells for large population mechanical phenotyping *Proc. Natl Acad. Sci. USA* **109** 7630–5
- [5] Tse H T K, Gossett D R, Moon Y S, Masaeli M, Sohsman M, Ying Y, Mislick K, Adams R P, Rao J and Di Carlo D 2013 Quantitative diagnosis of malignant pleural effusions by single-cell mechanophenotyping *Sci. Transl. Med.* **5** 212ra163
- [6] Dudani J S, Gossett D R, Tse H T K and Di Carlo D 2013 Pinched-flow hydrodynamic stretching of single-cells *Lab Chip* **13** 3728–34
- [7] Hou H W, Li Q S, Lee G Y H, Kumar A P, Ong C N and Lim C T 2009 Deformability study of breast cancer cells using microfluidics *Biomed. Microdevices* **11** 557–64
- [8] Khan Z S and Vanapalli S A 2013 Probing the mechanical properties of brain cancer cells using a microfluidic cell squeezer device *Biomicrofluidics* **7** 011806
- [9] Byun S *et al* 2013 Characterizing deformability and surface friction of cancer cells *Proc. Natl Acad. Sci. USA* **110** 7580–5
- [10] Rosenbluth M J, Lam W A and Fletcher D A 2008 Analyzing cell mechanics in hematologic diseases with microfluidic biophysical flow cytometry *Lab Chip* **8** 1062–70
- [11] Gabriele S, Benoliel A-M, Bongrand P and Théodoly O 2009 Microfluidic investigation reveals distinct roles for actin cytoskeleton and myosin II activity in capillary leukocyte trafficking *Biophys. J.* **96** 4308–18
- [12] Guan G, Chen P C Y, Peng W K, Bhagat A A, Ong C J and Han J 2012 Real-time control of a microfluidic channel for size-independent deformability cytometry *J. Micromech. Microeng.* **22** 105037
- [13] Adamo A, Sharei A, Adamo L, Lee B, Mao S and Jensen K F 2012 Microfluidics-based assessment of cell deformability *Anal. Chem.* **84** 6438–43
- [14] Mak M and Erickson D 2013 A serial micropipette microfluidic device with applications to cancer cell repeated deformation studies *Integr. Biol.* **5** 1374–84
- [15] Ji Q-Q, Du G-S, van Uden M J, Fang Q and den Toonder J M J 2013 Microfluidic cytometer based on dual photodiode detection for cell size and deformability analysis *Talanta* **111** 178–82
- [16] Ruths M and Israelachvili J N 2008 Surface forces and nanorheology of molecularly thin films *Nanotribology and Nanomechanics: An Introduction* ed B Bhushan (Berlin: Springer) pp 417–515
- [17] Tsai C D, Sakuma S, Arai F and Kaneko M 2014 A new dimensionless index for evaluating cell stiffness-based deformability in microchannel *IEEE Trans. Biomed. Eng.* **61** 1187–95
- [18] Pereira P, Valignat M-P, Bico J and Théodoly O 2013 Single cell rheometry with a microfluidic constriction: quantitative control of friction and fluid leaks between cell and channel walls *Biomicrofluidics* **7** 024111
- [19] Maloney J M and Van Vliet K J 2014 Chemoenvironmental modulators of fluidity in the suspended biological cell *Soft Matter* **10** 8031–42
- [20] Moeendarbary E and Harris A R 2014 Cell mechanics: principles, practices, and prospects *Wiley Interdiscip. Rev.: Syst. Biol. Med.* **6** 371–88
- [21] Sarimollaoglu M, Nedosekin D A, Simanovsky Y, Galanzha E I and Zharov V P 2011 *In vivo* photoacoustic time-of-flight

- velocity measurement of single cells and nanoparticles *Opt. Lett.* **36** 4086–8
- [22] Lim C T, Zhou E H and Quek S T 2006 Mechanical models for living cells—a review *J. Biomech.* **39** 195–216
- [23] Stone H A 1994 Dynamics of drop deformation and breakup in viscous fluids *Annu. Rev. Fluid Mech.* **26** 65–102
- [24] Bathe M, Shirai A, Doerschuk C M and Kamm R D 2002 Neutrophil transit times through pulmonary capillaries: the effects of capillary geometry and fMLP-stimulation *Biophys. J.* **83** 1917–33
- [25] Abkarian M, Faivre M and Stone H A 2006 High-speed microfluidic differential manometer for cellular-scale hydrodynamics *Proc. Natl Acad. Sci. USA* **103** 538–42
- [26] Vanapalli S A, Banpurkar A G, van den Ende D, Duits M H G and Mugele F 2009 Hydrodynamic resistance of single confined moving drops in rectangular microchannels *Lab Chip* **9** 982–90
- [27] Cartas-Ayala M A and Karnik R 2014 Time limitations and geometrical parameters in the design of microfluidic comparators *Microfluid. Nanofluid.* **17** 359–73
- [28] Abkarian M, Faivre M, Horton R, Smistrup K, Best-Popescu C A and Stone H A 2008 Cellular-scale hydrodynamics *Biomed. Mater.* **3** 034011
- [29] Tso C L et al 2000 Androgen deprivation induces selective outgrowth of aggressive hormone-refractory prostate cancer clones expressing distinct cellular and molecular properties not present in parental androgen-dependent cancer cells *Cancer J.* **6** 220–33
- [30] Hashimoto M, Garstecki P, Stone H A and Whitesides G M 2008 Interfacial instabilities in a microfluidic Hele-Shaw cell *Soft Matter* **4** 1403–13
- [31] El-Hamouz A 2007 Effect of surfactant concentration and operating temperature on the drop size distribution of silicon oil water dispersion *J. Dispersion Sci. Technol.* **28** 797–804
- [32] Xia Y and Whitesides G M 1998 Soft lithography *Annu. Rev. Mater. Sci.* **28** 153–84
- [33] Hochmuth R M 2000 Micropipette aspiration of living cells *J. Biomech.* **33** 15–22
- [34] Guo Q, Park S and Ma H 2012 Microfluidic micropipette aspiration for measuring the deformability of single cells *Lab Chip* **12** 2687–95
- [35] Hur S C, Henderson-MacLennan N K, McCabe E R B and Di Carlo D 2011 Deformability-based cell classification and enrichment using inertial microfluidics *Lab Chip* **11** 912–20
- [36] Fuerstman M J, Lai A, Thurlow M E, Shevkoplyas S S, Stone H A and Whitesides G M 2007 The pressure drop along rectangular microchannels containing bubbles *Lab Chip* **7** 1479–89
- [37] Bico J and Quéré D 2002 Self-propelling slugs *J. Fluid Mech.* **467** 101–27
- [38] Tsai M A, Frank R S and Waugh R E 1993 Passive mechanical behavior of human neutrophils: power-law fluid *Biophys. J.* **65** 2078–88
- [39] Ho B P and Leal L G 1975 The creeping motion of liquid drops through a circular tube of comparable diameter *J. Fluid Mech.* **71** 361–83
- [40] Tao J and Sun S X 2015 Active biochemical regulation of cell volume and a simple model of cell tension response *Biophys. J.* **109** 1541–50
- [41] Kavehpour H P and McKinley G H 2004 Tribo-rheometry: from gap-dependent rheology to tribology *Tribol. Lett.* **17** 327–35
- [42] Stokes J R, Boehm M W and Baier S K 2013 Oral processing, texture and mouthfeel: from rheology to tribology and beyond *Curr. Opin. Colloid. Interface* **18** 349–59
- [43] Vitkova V, Mader M and Podgorski T 2004 Deformation of vesicles flowing through capillaries *Europhys. Lett.* **68** 398
- [44] Li Y, Kumacheva E and Ramachandran A 2013 The motion of a microgel in an axisymmetric constriction with a tapered entrance *Soft Matter* **9** 10391–403
- [45] Li Y, Sar O S, Ramachandran A, Panyukov S, Rubinstein M and Kumacheva E 2015 Universal behavior of hydrogels confined to narrow capillaries *Sci. Rep.* **5** 17017
- [46] Xu W, Mezencev R, Kim B, Wang L, McDonald J and Sulchek T 2012 Cell stiffness is a biomarker of the metastatic potential of ovarian cancer cells *PLoS One* **7** e46609
- [47] Guck J et al 2005 Optical deformability as an inherent cell marker for testing malignant transformation and metastatic competence *Biophys. J.* **88** 3689–98
- [48] Katsantonis J, Tosca A, Koukouritaki S B, Theodoropoulos P A, Gravanis A and Stournarasy C 1994 Differences in the G/total actin ratio and microfilament stability between normal and malignant human keratinocytes *Cell Biochem. Funct.* **12** 267–74
- [49] Coffey D S 2002 Nuclear matrix proteins as proteomic markers of preneoplastic and cancer lesions *Clin. Cancer Res.* **8** 3039–45
- [50] He S, Dunn K L, Espino P S, Drobic B, Li L, Yu J, Sun J-M, Chen H Y, Pritchard S and Davie J R 2008 Chromatin organization and nuclear microenvironments in cancer cells *J. Cell. Biochem.* **104** 2004–15
- [51] Yogeewaran G and Salk P L 1981 Metastatic potential is positively correlated with cell surface sialylation of cultured murine tumor cell lines *Science* **212** 1514–6
- [52] Coughlin M F, Bielenberg D R, Lenormand G, Marinkovic M, Waghorne C G, Zetter B R and Fredberg J J 2013 Cytoskeletal stiffness, friction, and fluidity of cancer cell lines with different metastatic potential *Clin. Exp. Metastasis* **30** 237–50
- [53] Kollmannsberger P and Fabry B 2011 Linear and nonlinear rheology of living cells *Annu. Rev. Mater. Res.* **41** 75–97
- [54] Lange J R, Steinwachs J, Kolb T, Lautscham L A, Harder I, Whyte G and Fabry B 2015 Microconstriction arrays for high-throughput quantitative measurements of cell mechanical properties *Biophys. J.* **109** 26–34
- [55] Suresh S 2007 Biomechanics and biophysics of cancer cells *Acta Biomater.* **3** 413–38
- [56] Suresh S, Spatz J, Mills J P, Micoulet A, Dao M, Lim C T, Beil M and Seufferlein T 2005 Connections between single-cell biomechanics and human disease states: gastrointestinal cancer and malaria *Acta Biomater.* **1** 15–30
- [57] Li Q S, Lee G Y H, Ong C N and Lim C T 2008 AFM indentation study of breast cancer cells *Biochem. Biophys. Res. Commun.* **374** 609–13
- [58] Lekka M, Pogoda K, Gostek J, Klymenko O, Prauzner-Bechcicki S, Wiltowska-Zuber J, Jaczewska J, Lekki J and Stachura Z 2012 Cancer cell recognition—mechanical phenotype *Micron* **43** 1259–66
- [59] Fuhrmann A, Staunton J R, Nandakumar V, Banyai N, Davies P C W and Ros R 2011 AFM stiffness nanotomography of normal, metaplastic and dysplastic human esophageal cells *Phys. Biol.* **8** 015007
- [60] Cross S E, Jin Y S, Rao J and Gimzewski J K 2007 Nanomechanical analysis of cells from cancer patients *Nat. Nanotechnol.* **2** 780–3
- [61] Cross S E, Jin Y-S, Tondre J, Wong R, Rao J Y and Gimzewski J K 2008 AFM-based analysis of human metastatic cancer cells *Nanotechnology* **19** 384003
- [62] Prabhune M, Belge G, Dotzauer A, Bullerdiel J and Radmacher M 2012 Comparison of mechanical properties of normal and malignant thyroid cells *Micron* **43** 1267–72
- [63] Darling E M, Zauscher S, Block J A and Guilak F 2007 A thin-layer model for viscoelastic, stress-relaxation testing of cells using atomic force microscopy: Do cell properties reflect metastatic potential? *Biophys. J.* **92** 1784–91
- [64] Faria E C, Ma N, Gazi E, Gardner P, Brown M, Clarke N W and Snook R D 2008 Measurement of elastic properties of prostate cancer cells using AFM *Analyst* **133** 1498–500
- [65] Wu Z Z, Zhang G, Long M, Wang H B, Song G B and Cai S X 2000 Comparison of the viscoelastic properties of normal hepatocytes and hepatocellular carcinoma cells under cytoskeletal perturbation *Biorheology* **37** 279–90
- [66] Wu H W, Kuhn T and Moy V T 1998 Mechanical properties of L929 cells measured by atomic force microscopy: effects of anticytoskeletal drugs and membrane crosslinking *Scanning* **20** 389–97